

See discussions, stats, and author profiles for this publication at: <https://www.researchgate.net/publication/262644779>

High-throughput rare cell separation from blood samples using steric hindrance and inertial microfluidics

ARTICLE in LAB ON A CHIP · MAY 2014

Impact Factor: 6.12 · DOI: 10.1039/c3lc51384j · Source: PubMed

CITATIONS

5

READS

18

9 AUTHORS, INCLUDING:



[Chao Ma](#)

Northwest A & F University

12 PUBLICATIONS 22 CITATIONS

[SEE PROFILE](#)



[Jian-Chun Wang](#)

Shandong Academy of Sciences

33 PUBLICATIONS 378 CITATIONS

[SEE PROFILE](#)



[Juan Xu](#)

Northwest A & F University

28 PUBLICATIONS 161 CITATIONS

[SEE PROFILE](#)



[Long Pang](#)

Northwest A & F University

9 PUBLICATIONS 49 CITATIONS

[SEE PROFILE](#)

Cite this: *Lab Chip*, 2014, **14**, 2525–2535

High-throughput rare cell separation from blood samples using steric hindrance and inertial microfluidics†

Shaofei Shen,^a Chao Ma,^b Lei Zhao,^b Yaolei Wang,^a Jian-Chun Wang,^a Juan Xu,^a Tianbao Li,^a Long Pang^b and Jinyi Wang^{*ab}

The presence and quantity of rare cells in the bloodstream of cancer patients provide a potentially accessible source for the early detection of invasive cancer and for monitoring the treatment of advanced diseases. The separation of rare cells from peripheral blood, as a “virtual and real-time liquid biopsy”, is expected to replace conventional tissue biopsies of metastatic tumors for therapy guidance. However, technical obstacles, similar to looking for a needle in a haystack, have hindered the broad clinical utility of this method. In this study, we developed a multistage microfluidic device for continuous label-free separation and enrichment of rare cells from blood samples based on cell size and deformability. We successfully separated tumor cells (MCF-7 and HeLa cells) and leukemic (K562) cells spiked in diluted whole blood using a unique complementary combination of inertial microfluidics and steric hindrance in a microfluidic system. The processing parameters of the inertial focusing and steric hindrance regions were optimized to achieve high-throughput and high-efficiency separation, significant advantages compared with existing rare cell isolation technologies. The results from experiments with rare cells spiked in 1% hematocrit blood indicated >90% cell recovery at a throughput of 2.24×10^7 cells min⁻¹. The enrichment of rare cells was $>2.02 \times 10^5$ -fold. Thus, this microfluidic system driven by purely hydrodynamic forces has practical potential to be applied either alone or as a sample preparation platform for fundamental studies and clinical applications.

Received 13th December 2013,
Accepted 21st March 2014

DOI: 10.1039/c3lc51384j

www.rsc.org/loc

Introduction

Compared with surgical biopsies using fresh tissue, blood examination is less invasive and easier to routinely use for various health tests due to the accessibility and convenience of blood collection.¹ In addition, some low-abundance rare cells, such as leukemic cells and circulating tumor cells (CTCs), are found in the peripheral blood of cancer patients.² The presence and quantity of these rare cells are highly correlated with cancer metastasis and treatment analysis.^{2,3} In particular, 90% of all cancer-related deaths are caused by cancer metastasis. However, primary tumor sampling cannot promptly and accurately reflect the actual metastatic conditions or recurrence of cancer at an early stage,^{4,5} indicating an emerging need to precisely separate and detect rare cells that serve as representative surrogate tumor biomarkers for

real-time monitoring and personalized therapy. The availability of blood sample assays as a “virtual and real-time liquid biopsy” is beneficial for rare cell enumeration and characterization with respect to biological properties using current techniques. Thus, this process has been envisioned to replace conventional tissue biopsies of metastatic tumors and to revolutionize cancer diagnosis and treatment monitoring.⁶ However, processing and analyzing low-abundance rare cells from peripheral blood (~ 1 to 100 rare cells per 10^9 blood cells) present an obvious challenge because of the complex nature of blood and the rarity of target cells, similar to fishing for a needle in a haystack.^{2,6} Thus, a highly specialized separation or enrichment step is necessary to harvest high-purity and viable rare cells suitable for subsequent downstream (molecular) analysis.⁷

Current conventional macroscale approaches for rare cell fishing from blood samples are limited to labor-intensive, inefficient, and high-cost methods, such as physical filtration and density gradient centrifugation, or combined with red blood cell lysis for extracting mononuclear cells, immunomagnetic-assisted cell sorting, and fluorescence-activated cell sorting. These techniques are further complicated by the requirement for multiple batch complex procedures that result in cell

^aCollege of Science, Northwest A&F University, Yangling, Shaanxi, 712100, China.
E-mail: jywang@nwsuaf.edu.cn; Fax: +86 298 708 2520; Tel: +86 298 708 2520

^bCollege of Veterinary Medicine, Northwest A&F University, Yangling, Shaanxi, 712100, China

† Electronic supplementary information (ESI) available: Materials and methods, supplementary Fig. S1–S13 and Tables S1 and S2. See DOI: 10.1039/c3lc51384j

contamination or substantial loss of cancer cells, lack of efficiency and specificity due to the extremely low number of rare cells, and identification interference caused by aggressive rare cell subpopulations with reduced expression of epithelial markers; the latter phenomenon is ascribed to the epithelial-mesenchymal transition, which may underestimate the actual number of rare cells present in the bloodstream, giving rise to wrong expectations in clinical studies.^{8–10} Thus, simpler, less expensive, and more efficient techniques must be developed to separate and enrich sensitive rare cells from blood samples conveniently and rapidly for subsequent analysis in tumor research and clinical diagnostics.

With the rapid progress of promising microfluidic technologies, much attention in the field of blood analysis has been directed to microfluidic devices due to their small scale, simplicity of fabrication and automation, and excellent performance in controlling the blood microenvironment and processing complex blood cells.^{6,11–13} Furthermore, isolated rare cells can be used for subsequent on-chip cell culture or downstream (molecular) analysis as part of the rare cell separation process, eliminating the intermediate operation steps and accelerating the overall rare cell characterization procedures required in macroscale approaches.¹¹ Microfluidic-based rare cell separation systems have been increasingly studied with various proposed rare cell isolation mechanisms: cell-affinity micro-chromatography,¹⁴ cellular biophysics-based isolation,¹⁵ magnetic forces,¹⁶ and dielectrophoresis.¹⁷ However, a major limitation of on-chip blood processing for the analysis of rare cells is low processing throughput ($<10^6$ cells min^{-1}), either because of low operational flow rates or high whole blood viscosity, making them unsuitable for processing rare cell separation in clinical blood samples.²

Researchers have shown high-speed and precise particle/cell manipulation focuses at distinct positions in microchannels (henceforth known as inertial microfluidics) using inertial forces intrinsic to particle motion in confined channel flows.^{18–20} The throughput of hydrodynamic sorting techniques based on inertial microfluidics is very high without the application of external forces, and thus, may be suitable for rare cell separation from blood samples containing large numbers of various cells. Therefore, in our initial efforts, we attempted to construct a simple hydrodynamic method for particle/cell separation by introducing inertial microfluidics in a microfluidic device, in which contracting and expanding channels in turns and series were used to create multi-orifice flow fractionation (MOFF). Theoretically, this kind of device has greater potential for cell separation in a high-throughput manner than other microfluidic separators, and can be easily combined with either upstream or downstream applications to construct more complex lab-on-a-chip systems for addressing medical and biological issues. However, the high-purity separation of rare cells from complex human blood using only inertial microfluidics remains challenging. This difficulty may be due to the fact that malignant tumor cells, different from benign tumor cells, have irregular shapes and can grow rapidly.²¹ Moreover, different rare cell types and

different rare cell sub-types lead to cells possessing different characteristics, such as variations in size, shape and viscoelastic rheological properties.²² Studies have demonstrated that the use of steric hindrance separation techniques has great potential in cell separation. To date, various steric hindrance-based microfluidic devices have been developed, such as dead-end or crossflow filtration barrier devices,^{23–25} a dynamic microchannel device,²⁶ a multi-obstacle architecture filter device¹⁴ and a microfluidic funnel ratchets device.²⁷ These efforts have greatly enhanced rare cell separation. However, steric hindrance-based devices are often clogged during direct processing of complex blood samples, which complicates the process for obtaining statistically and quantitatively significant data and for further clinical applications.

Based on the analysis above, we present a multistage microfluidic device by combining inertial microfluidics with steric hindrance in turn. The use of inertial microfluidics can efficiently divide target cells and other cells into different groups and guide their movement in their respective trajectories. When the cells in different movement trajectories enter the steric hindrance region, masses of non-target cells are removed with the help of inertial microfluidics and a primary steric hindrance unit, greatly eliminating the blockage problem in the subsequent steric hindrance separation. To further purify the target cells, an isosceles trapezoid-shaped pillar array railing (μ ITPAR) functioning as a second steric hindrance unit was also integrated in the steric hindrance region, functioning as a re-focusing and re-purifying unit. We first investigated the separation mechanisms and performance of the designed device using theoretical calculations and fluorescence-labeled microspheres. Simultaneously, the optimal conditions for cell separation were also explored. Afterward, the removal of blood cells and the enrichment of tumor cells (MCF-7 and HeLa cells) and leukemic (K562) cells spiked in diluted whole blood was performed using the optimized microfluidic device.

Experimental

More detailed information on the materials and methods used can be found in the ESI.†

Device design

The device comprised four functional regions: (i) a filter region, (ii) an inertial focusing region, (iii) an inertial separation region, and (iv) a steric hindrance region. Fig. 1 shows a schematic of the microfluidic device structure and the high-throughput separation processes of rare cells in the microfluidic device. The use of the designed filter region (Fig. 1A), which effectively prevents subsequent channel clogging caused by cell aggregates or foreign debris, was critical in handling a high volume of blood samples.²⁸ The inertial focusing region (Fig. 1B) was composed of 80 repeated contraction/expansion channel units with a total length of 2.4 cm. The contraction and the expansion channels were both 150 μm long. Each expansion channel had a width of

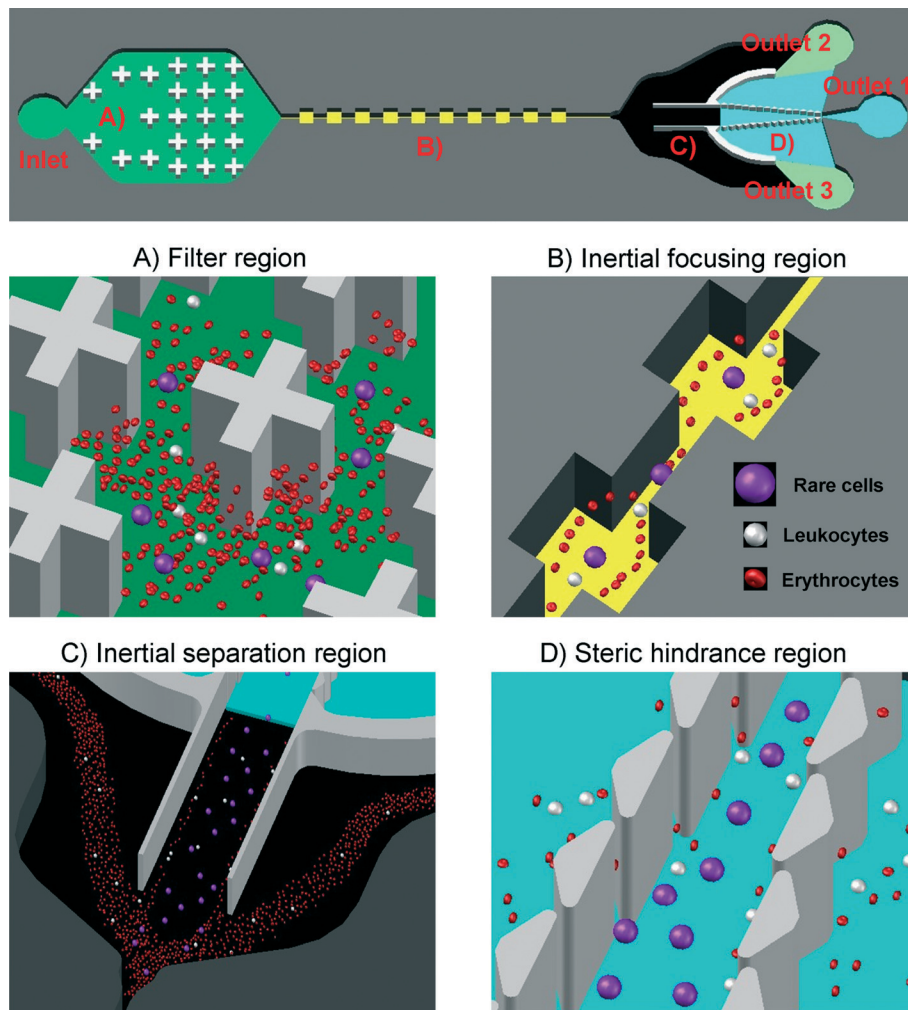


Fig. 1 Schematic diagram of the designed microfluidic device for rare cell isolation using steric hindrance and inertial microfluidics. The filter region (A) can effectively block foreign debris to avoid downstream clogging in microchannels. Under the influence of inertial lift forces and unique secondary flow in the inertial focusing region (B), relatively larger rare cells and a few blood cells pass through the center channel of the inertial separation region (C) and enter the steric hindrance region (D), whereas most blood cells exit through outlets 2 and 3. Subsequently, based on cell size and deformability in the steric hindrance region, the isosceles trapezoid-shaped pillar array railing (μ ITPAR) can further remove the unseparated blood components and enrich rare cells through outlet 1.

180 μm , whereas the contraction channel was designed in three different dimensions, 30, 60, and 90 μm , to investigate the focusing effect of the inertial focusing region. The height of the channels and microstructures of the device were all 57 μm . The main channel in the inertial separation region (Fig. 1C) was split into two side channels and one central channel by the steric hindrance structures. The two side channels were respectively connected with outlets 2 and 3 for removing small-sized cells (blood cells). The central channel was connected with outlet 1 for collecting large-sized target cells (rare cells). The expansion-shaped design with rapidly increasing angle, an important parameter for controlling separation amplification in the inertial separation region, promoted the shift of the particle/cell equilibrium position to the centerline.²⁹ The steric hindrance region (Fig. 1D) involving periodically spaced isosceles trapezoid-shaped pillars (for a detailed description of the designed devices (devices 1, 2,

and 3), see Fig. S1 and Table S1 in the ESI†) removed the unseparated blood components to improve target cell separation efficiency.

Cell viability assay

Cell viabilities before and after isolation were assessed by using a common acridine orange (AO) and propidium iodide (PI) double-staining protocol.³⁰ After removing the growth medium and rinsing with PBS, the AO/PI (5 $\mu\text{g mL}^{-1}$ in PBS) staining solution was introduced into the cell samples, and the staining process was performed for 10 min at room temperature. Afterward, PBS was introduced for 15 min as a final rinse.

Experimental setup

During each experiment, the microsphere/cell sample was pumped into the microfluidic device at varying channel

Reynolds numbers using a syringe pump (Longer pump, LSP01-1A) to generate a stable and continuous microflow. A 10 mL syringe was connected to the inlet (diameter: 2 mm) of the device using Tygon tubing (internal diameter: 0.42 mm; length: 25 cm). Prior to use, the device system was initially irradiated with UV light for 1 h, and then sequentially rinsed with 70% ethanol, followed by ultra-purified water and PBS working buffer.

Microscopy and image analysis

An inverted microscope (Olympus, CKX41) with a charge coupled device camera (Olympus, DP72) and a mercury lamp (Olympus, URFLT50) was used to obtain phase contrast and fluorescence images. Time-lapse images of the samples were obtained every 1 s. A total of 100 to 200 images were overlaid to create each averaged composite image. Image and data analyses were performed using Image-Pro® Plus 6.0 (Media Cybernetics, Silver Spring, MD) and SPSS 12.0 (SPSS Inc.) software, respectively. The results and error bars in the graphs are expressed as the mean \pm SD. Tests of data significance were performed using one-way analysis of variance (ANOVA).

Results and discussion

Theory and mechanism

In a microfluidic channel, the microspheres/cells suspended in a fluid are subjected to both inertial lift and viscous drag forces.¹⁹ Normally, we can interpret these occurrences using Reynolds number (Re), a dimensionless number that provides a measure of the ratio of the inertial forces to viscous force, characterizing the fluid dynamic phenomenon in the microchannel. In addition, we can describe the motion of the particles flowing through a microchannel using the particle Reynolds number (Re_p) as follows:

$$Re_p = Re_c \frac{d^2}{D_h^2} = \frac{\rho U_m d^2}{\mu D_h} \quad (1)$$

where Re_c is the channel Reynolds number, d is the particle diameter, ρ is the density of the fluid, μ is the dynamic viscosity of the fluid, and U_m is the maximum flow velocity in the channel. Moreover, the hydraulic diameter of the channel D_h is defined as follows:

$$D_h = \frac{2HW}{H+W} \quad (2)$$

where H and W are the height and width of the channel, respectively. Notably, Re_c uses maximum velocity instead of mean velocity, which is normally applied for Re . When $Re_p \gg 1$, the inertial lift force becomes a dominant parameter for driving the lateral migration of particles transverse to the fluid streamlines. Meanwhile, when $Re_p \ll 1$, the viscous drag force acting on the particle surface has an important role in longitudinal particle migration in the microfluidic channel.³¹

The size-based rigid particle separation in a radially asymmetric microchannel is operated by a combination of three fluid-mechanical lift forces: a shear-gradient-induced lift force, a wall effect-induced lift force, and a rotation-induced lift force.^{32,33} The equilibrium position of uniformly dispersed rigid particles is achieved by the balance of the three lift forces. The shear gradient-induced lift force produced by the parabolic laminar velocity profile in plane Poiseuille flow drives rigid particle migration toward the channel walls. However, when the rigid particles migrate closer to the channel wall, a counteracting wall-induced lift pushes these particles away, primarily because the fluid velocity and the asymmetric wake vorticity generated at the surface of the rigid particles induce higher pressure on the wall side than on the centerline side. After the two opposing lift forces balance each other, the rotation-induced lift force acts directionally on the rigid particles, generating a net force along the wall toward the channel center. The rigid particles then migrate to the stable equilibrium positions centered at the faces where limited spinning arises due to minimum shear rate.^{33,34} Deformable particles/cells can induce non-linear lateral migration due to deformation-induced lift force, aside from the nonlinearity related to the inertia of the fluid. Deformation-induced lift force is generated due to the matching of velocities and stresses at the deformable particle/cell interface. The magnitude of the lateral drift velocity and lift force is closely associated with the deformed shape of the particles/cells. Consequently, aside from the above three fluid-mechanical lift forces, the deformation-induced lift force will act on the deformed particles/cells to produce modified stable equilibrium positions.³⁵

Furthermore, size-based particle/cell separation in a multi-orifice microchannel is also driven by a secondary flow.^{34,36,37} As a consequence of a series of alternating narrow (contracting) and wide (expanding) channel geometries, a unique vortex will arise under low Re_c at the corners of the expansion channels. Interestingly, the presence of vortexes in an orifice channel is slightly different from that in the straight channel generated by high Re_c ,³⁸ and vastly different from that of the Dean vortex created in a curved channel at low Re_c (ref. 39) or the vortex created in asymmetrically structured microchannels.^{40,41} Vortex formation relies on several factors, including the ratio between contracting and expanding channel cross-section areas, angle and roundness of the orifice corner, surface roughness and fluid inertia.³¹ Notably, the fluid inertia depends primarily on Re_c . However, the increasing Re_c of the fluid increases the vortex size until the full-expansion region is occupied.⁴¹ To explore the vortex distribution in the microchannel of the current device, a numerical simulation was performed using ESI-CFD software under different experimental conditions.

As shown in Fig. S2A (ESI†), under different Re_c values, obvious vortex variations were observed along with the change of the fluid velocity in the vortex region. When $Re_c = 27.78$, a small vortex zone appeared near the entrance of the expansion chamber, occupying about 1/3 of the expansion channel cavity. A significant vortex zone was observed when $Re_c > 50$ due to

the suddenly expanding and contracting channel, covering almost half of the cavity area. When the Re_c was more than 72.22, the vortex flow expanded up to almost all of the cavity area. Quantitative analysis (Fig. S2B, ESI[†]) of the numerical simulation images showed that the fluid velocity in the vortex region increased with the increase in Re_c , and the position of the maximum flow velocity in the vortex zone became stable and uniform. With the increase in Re_c , the rising ratio of the flow velocity to the maximum flow velocity was the same along the direction of the microflow in the same position of the vortex region. However, upon reaching the maximum value of the ratio, the difference in the ratio decreased (Fig. S2C, ESI[†]). Consequently, we believe that the large size particles/cells form into a nearly linear pattern without severe sudden turns at a certain Re_c in the expansion chamber due to the presence of the vortex region, seeming to pass through a straight channel. We simulated the fluid velocity distribution of the inertial separation region with a specific range of Re_c (Fig. S3A and B, ESI[†]), which showed that the fluid velocity of the central channel region is higher than those of the two side channels at the same Re_c . Interestingly, we found that a lower ratio of flow velocity to maximum flow velocity can occur in the inertial separation region when Re_c was in the range 50 to 72.22 (Fig. S3A and C, ESI[†]). To the best of our knowledge, this phenomenon has not been reported previously. These results demonstrate that the fluid is inclined to flow toward the central channel region when the Re_c ranges from 50 to 72.22.

Mass conservation requires that the time rate of the change in mass in a control volume is balanced by the net mass that flows into the same control volume (inflow-outflow). The physical meaning is that the relative expansion rate of the fluid volume is equal to the relative decrease rate of the fluid density in any point of the incompressible flow field. Formula (2) (in the ESI[†]) is the continuity equation in differential form for incompressible flow, and the well-known integral form of the continuity equation can be expressed as follows:

$$\sum V_1 A_1 = \sum V_2 A_2 \quad (3)$$

where V_1 and V_2 are the mean velocity of the inlet and outlet channels, respectively, whereas A_1 and A_2 are the cross-sectional area of the inlet and outlet channels, respectively. The formula indicates that the mean velocity of any cross section is inversely proportional to the cross-sectional area for incompressible channel flow. A description of the fluid velocity between the isosceles trapezoid-shaped pillars would be helpful for this explanation (Fig. S1, ESI[†]). As shown in Fig. S4A (ESI[†]), we observed significant variations between the isosceles trapezoid-shaped pillars in the velocity magnitude distribution at $Re_c = 72.22$. As expected, numerical simulation results showed that the velocity quickly reached a peak, and then gradually declined after the minimum cross-sectional area increased between the pillars (Fig. S4B, ESI[†]). This result verified the integral form of continuity eqn (3). More importantly, the varying gaps between these pillars result in well-controlled constrictions for cells to pass or reorient, avoiding

the potential for nonspecific adsorption caused by prolonged contact between the cells and the pillars. Thus, the proposed structure of the current microfluidic device can prevent cell clogging and long-term cell deformation, which can help to achieve cell separation with high efficiency and high viability. The fillet radius of the isosceles trapezoid-shaped pillars is helpful in alleviating the cell damage caused by physical collisions (Fig. S1, ESI[†]).

Inertial separation of microspheres

The focusing mechanism of fluorescent microspheres in the inertial separation region (Fig. 1C) of the current device was studied first, which served as a theoretical foundation for the optimization of the cell separation conditions. Re_c ranging from 0.44 to 125.93 was applied based on the varying widths of the contraction channel (30, 60, and 90 μm) and a flow rate of 1 to 170 $\mu\text{L min}^{-1}$. The representative averaged composite images and fluorescence intensity corresponding to the red dotted lines are shown in Fig. 2 and S5 (ESI[†]), respectively, which indicate the microsphere (mimics of rare cells) distributions in the inertial separation region under various Re_c . When the width of the contraction channel was 90 μm , an obvious microsphere distribution band was not observed in the central region of the channel within the whole test range of Re_c (0.44 to 75.56). This observation may be due to the fact that no sharp width variation for the fluid between the expanding (180 μm) and contracting (90 μm) channels was present, resulting in a small area and velocity of the vortex. However, as Re_c increased, the high speed rotation of vortex flows generated two side cavities in the expansion channel, leading to the microsphere distribution inclining toward the central region of the channel. Particularly, in the case of $Re_c = 75.56$ ($Re_p = 3.28$), most microspheres passed through the central channel of the inertial separation region. This phenomenon was similar to those in low-aspect ratio (*i.e.*, height/width, ~0.5) rectangular microchannels, where the shear force along the microchannel perimeter is not uniform, leading to preferential microsphere focusing. Thus, strong lift forces acting on the microspheres push them to preferentially migrate along the microchannel height before further equilibrating along the microchannel width. Bhagat *et al.*⁴² explained that this experimental phenomenon occurred because the shear rate along the rectangular channel height is higher than that along the channel width.

For an aspect ratio of ~1 (width of the contraction channel = 60 μm), the microspheres were randomly dispersed throughout the inertial separation region (Fig. 2) due to the absence of microsphere equilibration at $Re_c = 0.56$ ($Re_p = 0.03$). In addition, increasing the flow to $Re_c = 11.11$ ($Re_p = 0.69$) caused two-band microspheres that were laterally and symmetrically focused at the inertial separation region. We believe that most microspheres only moved through the two sides of the cavities of the expansion channels downstream because either no or only a small vortex zone arose at low Re_c . The other important reason for this phenomenon is that the strong wall

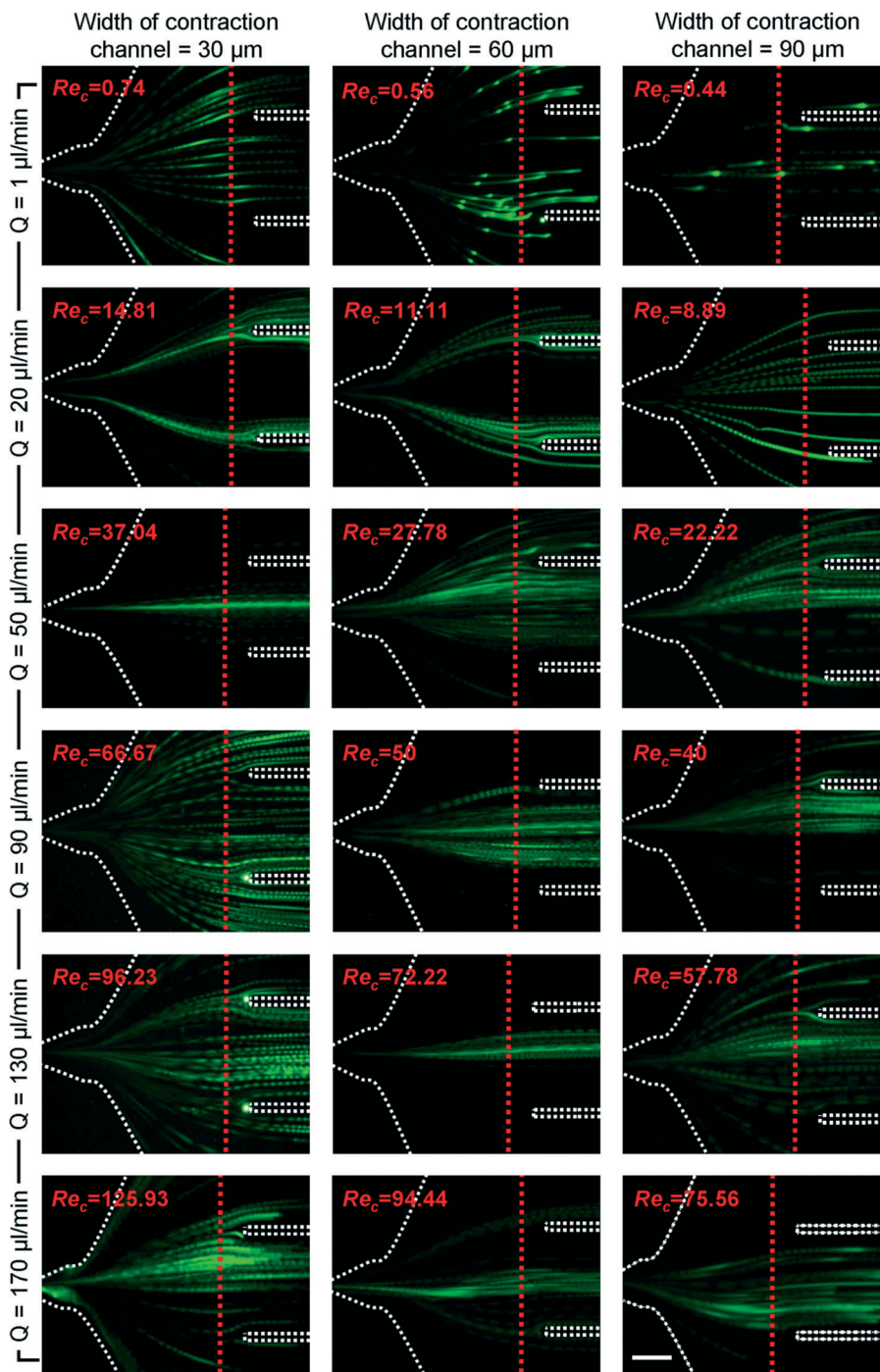


Fig. 2 One set of fluorescence photographs of fluorescence microsphere trajectories under various Re_c in the inertial separation region after passing through three different widths of contraction channels (30, 60, and 90 μm) in the inertial focusing region. The white dotted lines indicate the position of channel walls and elliptical columns. The red dotted lines were used to analyze fluorescence microsphere distributions at the same longitudinal positions. The analytical results are listed in Fig. S5 (ESI†). Scale bar, 200 μm .

effect-induced lift force in the contraction channel acted on the microspheres because their diameters were as large as one-quarter of the contraction channel width compared with that of the expansion channel. As the microspheres pass through the series of contraction and expansion channels, they gradually migrate to both sides of the passage. This phenomenon is

the major factor in realizing the separation of different-sized microspheres in a microchannel. Given the lack of geometrical effects from suddenly contracting and expanding channels, this clear microsphere distribution has rarely been achieved in a straight microchannel under the same conditions. As expected, the microsphere distribution in the inertial

separation region changed to pass through the central region of the channel with increasing Re_c ($Re_c = 27.78$ to 50), similar to those in a low-aspect ratio multi-orifice microchannel. Interestingly, the microspheres preferred to form a single band concentrated on the centerline of the central channel when $Re_c = 72.22$ ($Re_p = 4.51$) (Movie S1, ESI[†]). At a high Re_c of 94.44 ($Re_p = 5.90$), a three-band distribution of microspheres was observed in the inertial separation region; the microspheres were dispersed near the centerline and the side walls. The same phenomenon was observed in a straight noncircular channel.^{39,43} Notably, when the microspheres formed a nearly linear pattern without severe sudden turns because of the presence of the vortex region as they passed through a straight channel at high Re_c , the microspheres were influenced away from the walls due to the wall-induced lift force caused by another vortex generated near the walls. Thus, the three-band distribution phenomenon that occurred in the multi-orifice square channels can be similarly explained by the particle equilibrium alteration in a straight square channel. We concluded that these phenomena occurred because the vortex in the cavity region was fully developed and the velocity magnitude contouring at the vortex attained a critical value relative to the size of the microspheres and the setting of the microchannels. Thus, when passing through a series of alternating contracting (aspect ratio ~1) and expanding (aspect ratio <1) geometry channels, different-sized microspheres can be separated by forming into diverse band distribution patterns in the inertial separation region with an optimal critical value.

For an aspect ratio of ~2 (width of the contraction channel = 30 μm), the microsphere distributions were nearly consistent with those observed with an aspect ratio of ~1 when the flow rate was 1 $\mu\text{L min}^{-1}$ or 20 $\mu\text{L min}^{-1}$ due to the small difference in Re_c between the two different contraction channels (Table S2, ESI[†]). More specifically, the microspheres remained evenly distributed in the inertial separation region (Fig. 2), indicating little migration at $Re_c = 0.74$ ($Re_p = 0.10$). After increasing the flow rate to $Re_c = 14.81$ ($Re_p = 2.08$), the lift force permitted the microspheres to overcome the viscous drag. Aside from the influence of the vortex in the expansion channels, the lift force along the contraction channel width is four times greater than that along the channel height as a consequence of varying shear rates,⁴² which results in high lateral migration of microspheres along the channel width. Thus, at this flow rate ($Re_c = 14.81$; $Re_p = 2.08$), the microspheres began to migrate across the channel cross-section toward two equilibrium positions and focused near the sidewalls. Similar microsphere behavior was also observed in a high-aspect ratio (aspect ratio $\gg 1$) straight rectangular channel.^{33,42} However, the straight rectangular channel required higher Re_c compared with the multi-orifice channel due to the lack of geometrical effects from suddenly contracting and expanding channels. For $Re_c = 37.04$ ($Re_p = 5.21$), another obvious change was observed in the microsphere distribution due to the action of the vortex in the cavity region; a central microsphere band was concentrated on the centerline of the center channel region. For $Re_c > 66.67$ ($Re_p > 9.38$), the

microspheres were dispersed near the two sides of the channels and the central channel. In particular, two small vortex zones were formed near the initial part of the inertial separation region when $Re_c = 125.93$ ($Re_p = 17.71$). The trains of the microspheres were unstable and the spacing between the microspheres in the central and side channels was no longer uniform. The exact origin of this behavior remains unclear and warrants further investigation. However, we believe that the microsphere distributions were likely influenced by the high volume fraction of the microspheres in a high-aspect ratio multi-orifice channel. The movement of microspheres in the contraction channel was clearly affected as a result of the multibody interactions at high Re_c ; thus, a single-microsphere equilibrium position cannot be formed in the suddenly contracting and expanding narrow channels. The interactions between the microspheres were not negligible, and transient aggregation of closely spaced particles likely occurred in the narrow contraction channel at high Re_c ; the same phenomenon was observed by Chun and Ladd in a square duct at high Re_c .⁴³ These results indicated that low Re_c cannot induce microspheres to pass through the central channel of the inertial separation region and high Re_c can lead to excessive turbulence around the microspheres, so stable equilibrium positions cannot be produced. A single-microsphere band concentrated on the central channel can be formed at a moderate Re_c , with a suitable channel aspect ratio, and an appropriate microsphere volume fraction.

To precisely analyze the microsphere distribution characteristics, the fluorescence intensities of the distributed microspheres, which indirectly represent microsphere distribution (Fig. S5, ESI[†]), were analyzed. The fluorescence intensity along the red dotted lines (Fig. 2) was analyzed using Image-Pro Plus 6.0 software, from which only three kinds of Re_c (37.04, 50, and 72.22) were found to promote the formation of the microspheres into a single band in the central channel region (250 μm to 750 μm). However, in the imaging analysis, the fluorescence intensities of the well-focused fluorescence microspheres captured by the CCD camera were considerably brighter than the fluorescence intensities of the off-focus microspheres, resulting in poor accuracy in the measurement of fluorescence intensity magnitude.³¹ Therefore, microsphere recovery, defined as the percentage of microspheres successfully sorted from the total number of microspheres within the initial injected fraction, was calculated at specific ranges of Re_c . As shown in Table S2 (ESI[†]), the highest recovery (98.93%) for 30 μm contraction channels can be achieved at $Re_c = 37.04$ ($Re_p = 5.21$), the highest recovery (99.42%) for 60 μm contraction channels can be achieved at $Re_c = 72.22$ ($Re_p = 4.51$), and the highest recovery (88.32%) for 90 μm contraction channels can be achieved at $Re_c = 75.56$ ($Re_p = 3.28$). However, the optimum Re_p range for equally sized microspheres changed as the contraction channel dimensions changed (Table S2, ESI[†]). Overall, the optimum results for the 30 and 60 μm contraction channels are superior to existing inertial systems. Considering that the 30 μm contraction channels can easily lead to intermittent clogging problems and

cannot achieve stable performance, a contraction channel dimension of 60 μm and a value of Re_c ranging from 50 to 72.22 were chosen for the subsequent sample separation.

Inertial separation of cells

Cell experiments were first performed to investigate the effects of hematocrit (Hct) on the focusing of blood cells in the multi-orifice microchannel. Human blood is composed of the following three main types of cells: erythrocytes, leukocytes, and platelets. Erythrocytes or RBCs are highly deformable, discoid biconcave-shaped cells with diameters ranging from 6 μm to 8.5 μm and thicknesses ranging from 1.8 μm to 2.8 μm . Leukocytes or WBCs are deformable, nearly spherical cells with diameters larger than 6 μm to 10 μm (granulocytes: 10–15 μm ; lymphocytes: 6–15 μm ; monocytes: 12–20 μm). Platelets have diameters ranging from 1 μm to 3 μm . To achieve a high-separation purity of rare cells, inappropriately sized blood cells must be prevented from entering center outlet 1. Generally, whole blood (~40% Hct) is too viscous to achieve Newtonian fluid separation.⁴⁴ In addition, the high cell density of whole blood will result in increased cell-cell interaction and focusing imbalance. Thus, a dilution procedure for whole blood is necessary. However, working with high Hct is imperative to save time on processing and analysis. To determine the optimum Hct (minimum dilution) that can be processed in a microchannel without affecting the blood cell focusing, tests with diluted whole blood cells (0.5% to 8% Hct) were conducted under the optimum test conditions, which were determined through the above experiments on the inertial separation of fluorescent microspheres. To obtain clear photographic images of blood cells during the separation process, background images were captured at certain time intervals from the same site in the channel to allow background correction, wherein all pixels with the same value were removed. As a result, high-contrast composite images describing the blood cell equilibration variation were acquired (Fig. S6, ESI†). Fig. S6A and D in the ESI† show the blood cell equilibration position and corresponding light intensity assay, respectively, under different Hct conditions. A central cell-free layer developed for $\text{Re}_c = 72.22$ at Hct = 0.5%. However, as Hct increased to 2%, a clear central cell band was formed in the multi-orifice microchannel and the corresponding light intensity became stronger because of abundant cell-cell interactions and overlapping at the same Re_c (Fig. S6, ESI†). When Hct was increased to 8%, the width of the central cell band became wider than when Hct was 2%. Considering that RBCs comprise the majority of blood constituents, the intensity distribution primarily represents the RBC equilibration.⁴⁴ This phenomenon can be explained as follows: as the blood cell concentration increases, more blood cells attempt to occupy the same equilibrium positions spontaneously, leading to enhanced cell-cell interactions and greater focusing imbalance. In addition, the effect of high Re_c on blood cell equilibration variation at Hct = 2% was investigated, and the light intensity distribution across the

channel width was measured using the collected images (Fig. S6B and E, ESI†). The above results illustrate that the blood cell equilibration position is not stable at high Hct because of cell focusing imbalance caused by cell-cell interactions and irregular variation of channel resistances. In addition, as Re_c increases, the width of the central cell-free layer increases (Fig. S6E, ESI†). Based on the above results, 1% Hct was chosen for cell separation in the inertial microfluidic system. The results (Fig. S6C and F, ESI†) show that not all blood cells were focused in the equilibrium positions close to the channel sidewalls in a given channel length (2.4 cm) when $\text{Re}_c = 50$. However, $\text{Re}_c = 72.22$ can provide good focus for blood cells, forming a clear 60 μm (in width) central cell-free layer at Hct = 1% (the width was obtained by measuring the full width at half maximum (FWHM) of the distance between the two cell-occupied regions). As Re_c increases, the large inertial lift forces enable the cells to overcome the drag forces better, and more cells are induced to focus toward the channel sidewalls. Interestingly, when Re_c was increased to 94.44, three cell-band distributions with ~10 μm width were observed (Movie S2, ESI†). The width of the cell-bands was determined by measuring the FWHM of the region occupied by the blood cells. To our knowledge, this is the first illustration of three-band blood cell distribution in a multi-orifice microchannel at high Re_c . We concluded that this phenomenon occurred because the lateral migration of blood cells is influenced by inertial lift forces and unique secondary flow at high Re_c , and the equilibrium position lies on the center or corner of side walls similar to equilibrium alteration in a straight square channel.⁴² In addition, two side peaks that were 50 μm away from the channel sidewalls were observed to exhibit higher intensity than that of the central peak (Fig. S6F, ESI†), similar to a previous study in a straight microchannel.⁴²

Additionally, the optimum Re_c range was obtained by measuring blood cell trajectories in the inertial separation region at Hct = 1% (Fig. 3). Blood cells were spread out over a wide area and were inclined to concentrate on the centerline in the central channel region at a low Re_c ($\text{Re}_c \leq 27.78$) (Fig. 3). Thus, the highest peak representing the maximum light intensity of cells (Fig. S7, ESI†) was also located at the centerline of the central channel region. The longitudinal distribution width of blood cells in the central channel region became narrower from ~800 μm to ~600 μm as Re_c increased from 11.11 to 27.78. Meanwhile, a white region corresponding to a mass of red blood cells in the captured images appeared at $\text{Re}_c \leq 27.78$, which resulted from abundant cell-cell interactions and overlapping. As Re_c increased, the blood cells from the inertial focusing region became bifurcated ($\text{Re}_c = 50$), clearly split into two groups entering their respective side channels ($\text{Re}_c = 72.22$), and formed a three-band distribution ($\text{Re}_c = 94.44$) (Fig. 3). The formation of the three-band distribution at $\text{Re}_c = 94.44$ is unfavorable for separation because the rare cell enrichment efficiency will be decreased. Based on the above results, a Re_c of 72.22 was preliminarily chosen as the optimal condition for blood cell focusing in

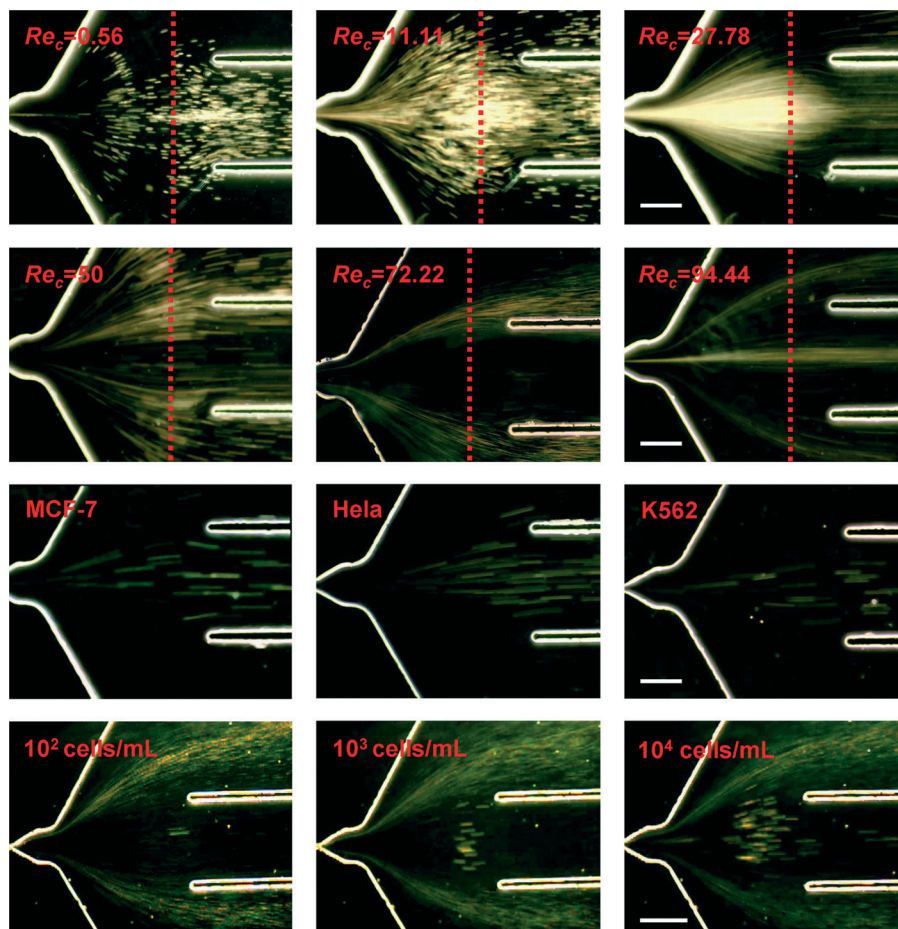


Fig. 3 Cell trajectories in the inertial separation region under various Re_c values. The first and second rows show blood cell trajectories under various Re_c values when Hct = 1%. The red dotted lines were used to analyze blood cell distributions at the same longitudinal positions. The analytical results are listed in Fig. S7 (ESI†). The third row shows different rare cell (MCF-7, HeLa, and K562 cells; 10^4 cells mL^{-1} in PBS working buffer) trajectories at $Re_c = 72.22$. The fourth row shows the trajectories of K562 cells at different concentrations (in 1% Hct blood) at $Re_c = 72.22$. In the study, the width of the contraction channel in the inertial focusing region is 60 μm . Scale bar, 200 μm .

the inertial separation region, which was also the optimum condition for the inertial focusing region.

In the case of the three rare cells MCF-7, K562, and HeLa, the optimum Re_c was used which was achieved from the separation of fluorescence microspheres in the earlier inertial separation experiment. Fig. 3 shows the MCF-7, HeLa, and K562 cell trajectories in the inertial separation region after flowing through the multi-orifice microchannel at $Re_c = 72.22$. The cell streamlines were finely focused in the central channel region. After conducting independent flow measurements of the rare cells, each kind of fluorescently labeled rare cell was spiked into unstained 40 \times diluted whole blood and subsequently used in Re_c measurements. Cells moving at high speeds could not be imaged well at extremely short exposure times because of their lower fluorescence intensities compared with the fluorescent microspheres, so only bright-field images permitting enhanced visualization were taken. Fig. 3 illustrates that K562 cells with different concentrations were successfully separated from 1% Hct blood, and almost all of

the low-concentration (10^2 cells mL^{-1}) K562 cells passed through the central channel region (Movie S3, ESI†). The above phenomenon can be explained as follows: the highly concentrated K562 cells attempt to occupy the same equilibrium positions spontaneously, resulting in focusing dispersion and ideal flow pattern disturbance caused by their surrounding flow field change. Consequently, we believe that when the multi-orifice microchannel is sufficiently longer (2.4 cm) than the narrow width of the channel (60 μm or 180 μm), the cell-cell interactions that affect cell focusing behavior and deteriorate separation efficiency cannot be disregarded even with 1% Hct blood cells. Similar results were obtained in a snake-shaped channel in a study by Tanaka.⁴⁵ These results suggested that aside from Re_c , the equilibrium positions of cells vary depending on their concentration and channel-to-cell size ratio (D_h/d).^{45,46} At low sample concentration, an equilibrium position driven from the interaction of drag force and inertial lift force moves toward the wall as Re_c increases. Afterward, at a constant Re_c , this equilibrium position shifts toward

the centerline as D_h/d decreases. Estimating the equilibrium position variation for a high-concentration sample in the multi-orifice microchannel is difficult. In addition to sample concentration, sample shape and deformability are also important factors affecting the equilibrium position.

Tumor cells not only have larger volume and cellular karyon but also have better deformability compared with solid microspheres.²² Furthermore, multicellular CTC clusters yielding important prognostic significance have been reported in clinical samples.^{6,40} Therefore, the equilibrium positions of tumor cells are different from rigid microparticles under the same separation conditions. More specifically, deformable cells experience deformation-induced lift force compared with rigid microspheres, and differently shaped cells may respond differently to inertial forces in the applied flow field.³⁵ In addition, unlike rigid microspheres whose sizes are evenly controlled, cells have a relatively wide size distribution (Fig. S8, ESI†). All the above issues limit the enrichment efficiency of rare cells in the inertial separation region. Therefore, a central channel with a width of 500 μm was used to collect the target cells efficiently and to avoid the loss of some small and irregular rare cells, especially CTC clusters. However, in the present case, this situation would collect more non-target blood cells, especially for some leukocytes, which have overlapping sizes with heterogeneous rare cells. It may also pose a contamination problem for the target cells and decrease the performance of the designed device. Therefore, in the current device, a steric hindrance structure was designed and connected with the central channel of the inertial separation region to achieve high-purity separation of rare cells.

Steric hindrance separation of microspheres and cells

Microsphere trajectories in the steric hindrance region were first measured under optimum conditions. In the case without μITPAR (Fig. 4A), when $Re_c = 27.78\text{--}50$, microspheres were distributed throughout the expansion region. A three-band microsphere distribution phenomenon was observed, which can be similarly explained by alteration of the microsphere equilibrium because of the sudden decrease in resistance in the two side-outlet regions (Fig. 1). The two empty spaces between the central band and the two side bands became wider as Re_c increased. However, when $Re_c = 72.22$, the empty spaces disappeared and the microspheres maintained a straight movement. The above results can be explained as follows: with increased $Re_c = 72.22$, the high-velocity microspheres spontaneously attempted to concentrate on the centerline equilibrium positions in the inertial separation region, so the subsequent resistance change in the steric hindrance region cannot change the direction of the microsphere motion within a short time. However, the width of the central band became wider than that of the inertial separation region (Fig. S9, ESI†), which is highly unfavorable for sample separation, especially for irregular cells. Therefore, in the current device, a unique combination of MOFF and μITPAR was used to achieve maximum target sample recovery. As shown in

Fig. 4B, at $Re_c = 27.78$ to 50 in device 1 (Table S1, ESI†), poorly focused microspheres were stopped by the μITPAR . The central band microsphere distribution became narrower and more concentrated on the centerline equilibrium positions as Re_c increased. When $Re_c = 72.22$, the microspheres tended to form a single band concentrated on the centerline in the steric hindrance region, consistent with the inertial focusing principle (Movie S4, ESI†). However, a few poorly focused microspheres were not immobilized in the gaps between microposts and were also guided along the micropost array rails into the final outlet at $Re_c = 72.22$ (short arrows in Fig. 4C). The above phenomenon can be explained as follows: the radius of fluorescent microspheres (7.5 μm) is larger than the line offset (5 μm), which promotes the movement of microspheres along the micropost array rails. Furthermore, the velocity vector of the microspheres is parallel to the direction of the centerline at the optimum Re_c (72.22), so microspheres entering the gaps between each two micropost pillars at a clogging angle is avoided. The obtained results are similar with previously reported findings.⁴⁷

Based on the observation of microsphere separation, the trajectories of MCF-7, HeLa, and K562 cells in the steric hindrance region after flowing through the inertial separation region were investigated (Fig. 4D). As discussed above, irregularly shaped rare cells, especially high-concentrations of rare cells, cannot form a single central band concentrated on the centerline of the steric hindrance region (Movie S5, ESI†). However, the microposts in the device can guide the poorly focused cells to move along the μITPAR , which improves cell recovery. In the case of mixed samples (*i.e.*, rare cells spiked in diluted whole blood), when the rare cells and unseparated blood cells from the inertial separation region entered the central channel of the steric hindrance region, the unseparated blood cells were filtered by the microfluidic array rails. In the current device, the minimum space (10 μm) between two pillars was designed to be smaller than the diameter of rare cells, but larger than the small or highly deformable blood cells. Therefore, after the steric hindrance separation the rare cells were transported through rails into center outlet 1, while other small or highly deformable blood cells transited into the two side-outlets (Fig. 4D). In addition, compared with traditional filtration techniques, the μITPAR used in the current device can effectively avoid the problem of clogging or jamming. Given that the fluid flow direction in traditional dead-end filtration is perpendicular to the filtration structures, some larger and stiffer samples cannot pass through the barriers, leading to clogging. By contrast, in the current device, the fluid flow direction is nearly parallel to the filtration rails, which prevents the problem of jamming. In addition, traditional dead-end filtrations limit the ability to achieve high-throughput separation. However, in the current device, a large number of blood cells were removed by inertial separation before entering the rail array region, eventually achieving high-throughput and high-efficiency separation.

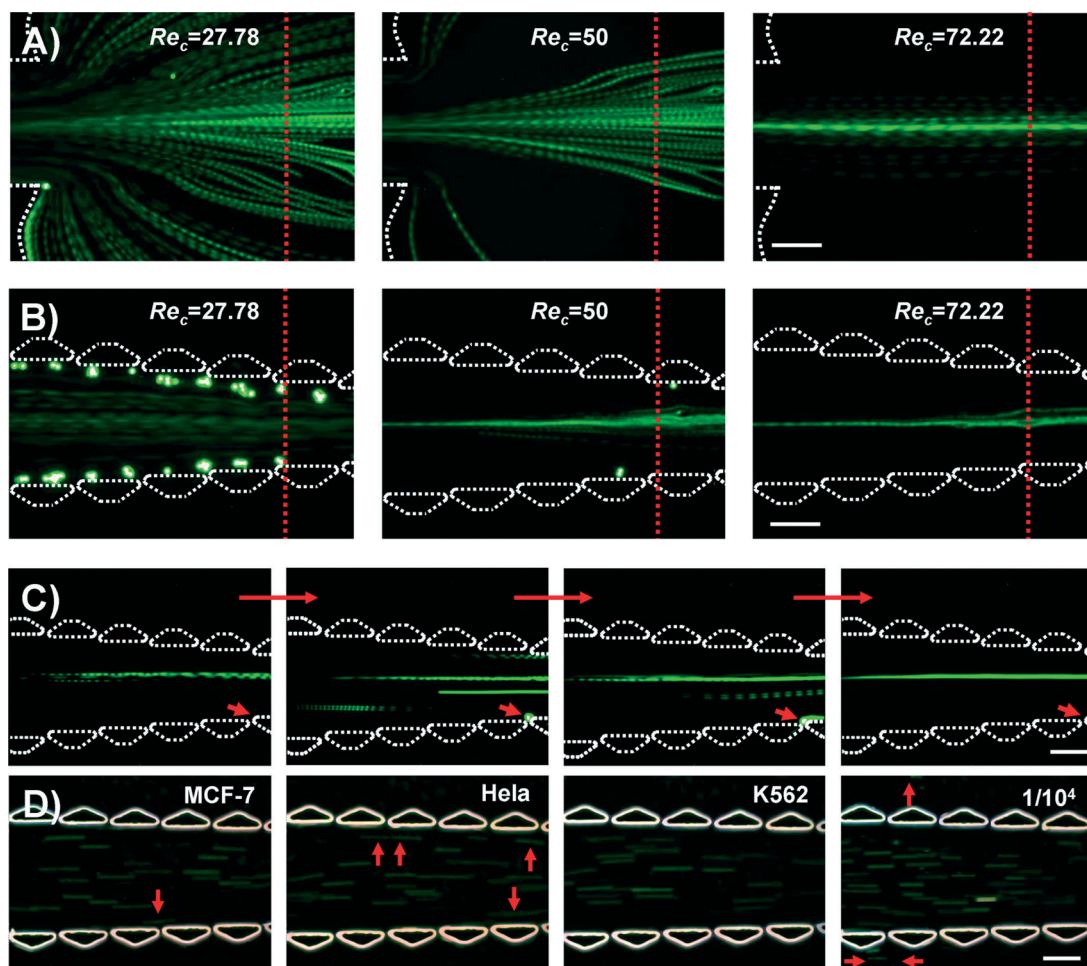


Fig. 4 Microsphere (A, B and C) and various cell (D) trajectories in the steric hindrance region. (A) and (B): microsphere trajectories under different Re_c in the steric hindrance region without (A) and with (B) the μ ITPAR structure. The red dotted lines were used to analyze fluorescence microsphere distributions at the same longitudinal positions. The analytical results are listed in Fig. S9 (ESI \dagger). (C) Sequential micrographs of microspheres which are railed without being immobilized in the steric hindrance region at $Re_c = 72.22$. The long red arrows represent the sequential direction of the micrographs. The short red arrows show that the poorly focused microspheres were well railed without moving away from the steric hindrance region (for the detailed process, see Movie S4, ESI \dagger). (D) From left to right: trajectories of rare cells (MCF-7, HeLa, and K562 cells; 10^4 cells mL^{-1} in PBS working buffer) and MCF-7 cells (spiked in 1% Hct blood; the MCF-7 cell to blood cell ratio is $1/10^4$) in the steric hindrance region at $Re_c = 72.22$. The red arrows indicate that the filtered cells were railed by the micropost array. Scale bar, 200 μ m.

Isolation efficiency and cell viability

To comprehensively evaluate the device performance, the isolation efficiency of each independent sample (microsphere, K562 cells, and blood cells) was calculated with different versions of the μ ITPAR (*i.e.*, devices 1, 2, and 3, Table S1 in ESI \dagger) with specific ranges of Re_c (Fig. S10, ESI \dagger). First, the collection efficiencies of microspheres were found to be greater than the collection efficiency of K562 cells under the same separation conditions regardless of the μ ITPAR pattern. As expected, these observations were ascribed to the existence of cellular heterogeneity in cell sizes and types (Fig. S8, ESI \dagger), which affected the quality of the separation. Additionally, compared with devices 2 and 3, device 1 can achieve a more preferable collection efficiency for microspheres/K562 cells. The reason is that the short line offset promotes the movement of microspheres/K562 cells along the micropost array

rails. Device 1 can effectively reduce blood cell recovery in center outlet 1 without affecting the target cell collection efficiency relative to the control groups, which agrees well with our observations on sample trajectories in the steric hindrance region. Finally, the optimum Re_c for blood cell separation is verified to be 72.22, which is similar to our previous observations on blood cell trajectories. Unfortunately, the maximum collection efficiency for high-concentrations (10^4 cells mL^{-1}) of K562 cells was achieved at $Re_c = 83.33$ (Fig. S10, ESI \dagger). Therefore, the collection efficiency of K562 cells at different concentrations spiked in diluted whole blood was measured under the two flow conditions, *i.e.*, $Re_c = 72.22$ and 83.33 (Fig. 5A). Unexpectedly, similar collection efficiencies for low-concentrations of K562 cells ($<10^3$ cells mL^{-1}) can be obtained under the two different Re_c conditions, possibly because of decreased interactions between rare cells at a low cell concentration, generating

preferable inertial focusing under a short and specific range of Re_c . Thus, tests for each independent cell sample (in this study, a $1/10^6$ ratio of rare cells-to-blood cells was used to mimic the low-abundance of rare cells in diluted whole blood) were conducted under optimum Re_c (*i.e.*, $Re_c = 72.22$) and high rare cell collection efficiency ($>90\%$) and enrichment efficiency ($>2.02 \times 10^5$ -fold) for the three rare cells MCF-7, HeLa, and K562 (Fig. 5B) were achieved. As expected, this enrichment efficiency is much higher than that ($>1.64 \times 10^3$ -fold) of the microfluidic system without a steric hindrance region (Fig. S11†). A set of representative images for leukemic cells input into the inlet and collected in the different outlets is shown in Fig. S12 (ESI†). In addition, the ability of the current device to isolate large MCF-7 cells (average diameter of approximately $18.8 \pm 2.3 \mu\text{m}$) was found to be more favorable ($94.9 \pm 2.69\%$ collection efficiency) than for the relatively small K562 cells (average diameter around $16.8 \pm 2.1 \mu\text{m}$) and HeLa cells (average diameter of approximately $14.6 \pm 2.8 \mu\text{m}$). The collection efficiencies of K562 and HeLa cells were almost similar, *i.e.*, $91.8 \pm 2.08\%$ for K562 cells and $90.2 \pm 4.39\%$ for HeLa cells. The reasons

for the different collection efficiencies of the three rare cells may be their deformability, which possibly exerted some secondary effects on cell separation, other than cell size, which requires further verification using the current integrated system. Although the current system has the ability to isolate a highly heterogeneous mix of rare cells, a small amount of rare cells (*e.g.*, HeLa cells) with diameters smaller than $10 \mu\text{m}$ are inevitably lost in the waste outlets (outlets 2 and 3).

Considering that some poorly focused rare cells underwent small deformations because of high shear stress, the viability and integrity of the collected cells must be considered. After separation, rare cell viability was determined by reseeding cells back into culture to observe their morphologies and the extent of proliferation. The results (Fig. S13, ESI†) show that the morphology and proliferation rate of the collected rare cells were analogous to the control cells, and no noticeable changes were observed. In addition, culture of sorted rare cells stained using CellTracker Green in a 96-well plate (Fig. 6) was successfully performed. Particular attention was given to the separated HeLa cells, demonstrating that the device can successfully separate aggregated cancer cells similar to CTC clusters despite high flow conditions (Fig. 6). This phenomenon may be caused by the short transit time within the channel, which prevents breakup of the cell clusters. Cell viability was further assessed using a common AO/PI double-staining protocol.^{30,48} As a result, $>92\%$ viable cells were retrieved for all three rare cells, indicating that high shear stress does not compromise cell viability (Fig. S14, ESI†). The obtained results confirm that the developed multistage technology exerts minimal effects on cell viability during the high-speed separation process. The obtained results also illustrate that the microfluidic device developed in this study has the potential to obtain high-purity and high-viability rare cells. In addition, unlike other types of microfluidic rare cell separation systems, which only allow on-chip growth of cells, inherently limiting their ability to couple with conventional biological assays or other downstream applications platforms, the present passive cell separation technique can achieve continuous sorting, allowing easy retrieval of rare cells that remain intact and viable. Therefore, this technique could be used for downstream rare cell analysis, such as cell culture, gene analysis, drug screening and cancer prognosis.

Conclusions

In this study, a passive multistage microfluidic device was developed using a unique combination of inertial microfluidics and steric hindrance. The serial complementary combination of the two different sorting methods achieved high-throughput and highly sensitive cell separation. The separation and focusing mechanisms of this microfluidic system were discussed using a comprehensive numerical model of velocity field fluctuations and experimental studies of fluorescence-labeled microspheres. As an actual application of this microfluidic system, tumor cells (MCF-7 and HeLa cells) and leukemic (K562) cells spiked into 1% Hct blood were successfully

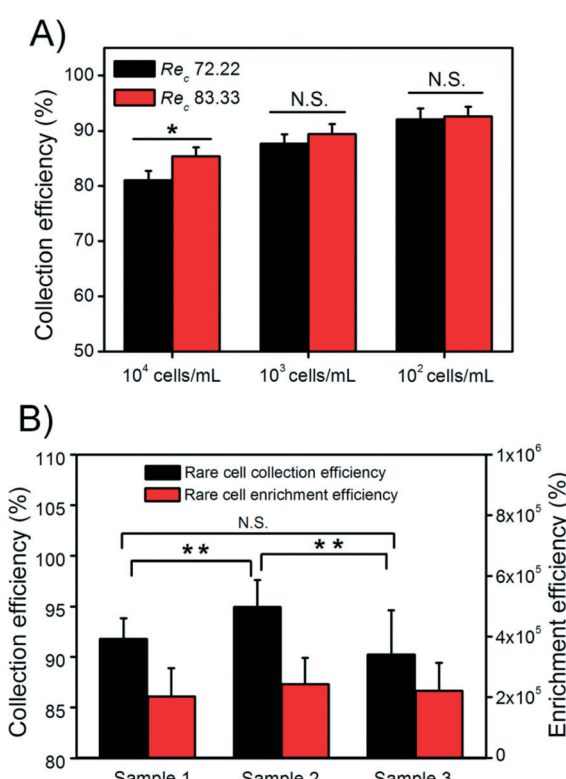


Fig. 5 Evaluation of the microfluidic system performance using rare cells (K562, MCF-7, and HeLa cells). (A) Comparison of the collection efficiency for different concentrations of K562 cells in diluted whole blood (1% Hct) under various flow conditions. (B) Statistical results of collection efficiency and enrichment efficiency of rare cells at a rare cell-to-blood cell ratio of $1/10^6$. Each type of independent rare cell spiked into diluted whole blood (sample 1, K562 cells; sample 2, MCF-7 cells; and sample 3, HeLa cells) was tested using optimum test conditions (1% Hct blood and $Re_c = 72.22$). Standard deviations deduced from ten parallel experiments are shown as the error bars, with the significance assessed by ANOVA. ** $P < 0.01$; * $P < 0.05$; N.S., not significant.

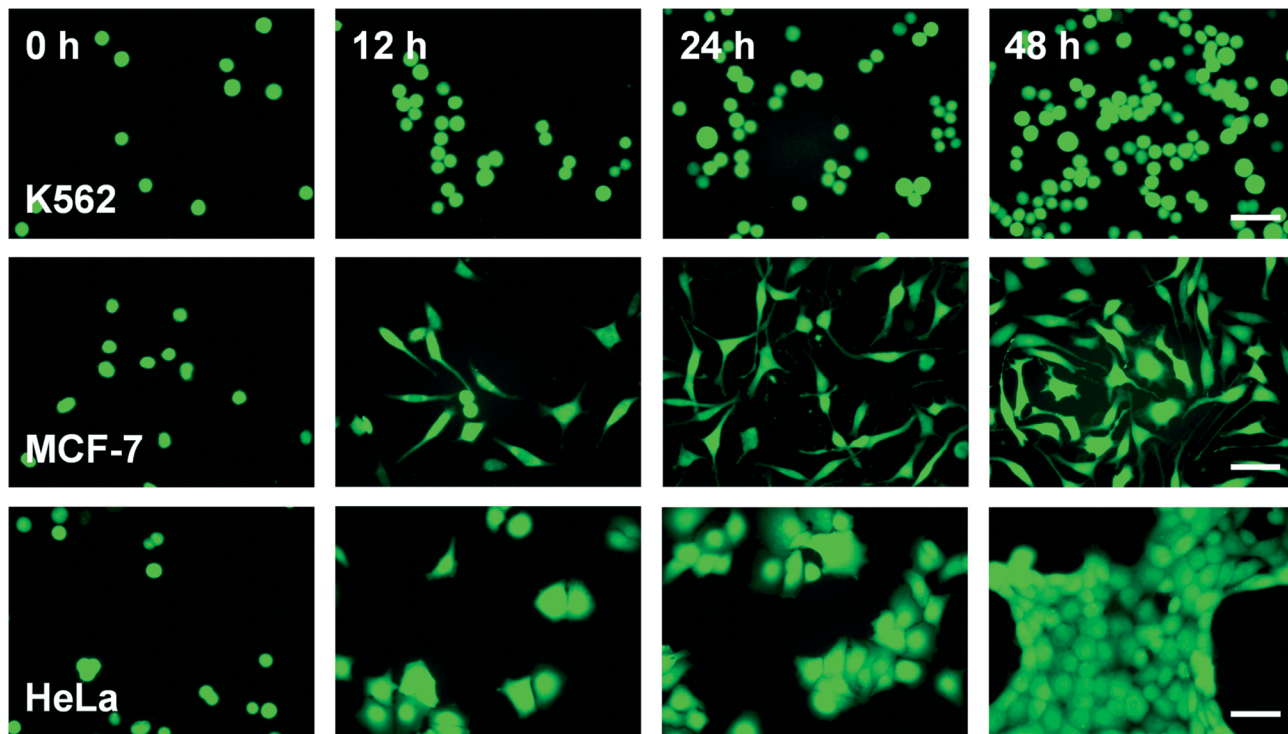


Fig. 6 Cellular viability assay of isolated rare cells (K562, MCF-7, and HeLa cells) by reseeding them back into culture for 48 h. In this study, the rare cells (10^4 cells mL^{-1} , spiked in 1% Hct blood) were all stained with CellTracker Green before separation to easily distinguish them from the blood cells. Scale bar, 50 μm .

Published on 21 March 2014. Downloaded on 18/10/2014 00:53:35.

separated with a throughput of 2.24×10^7 cells min^{-1} , cell recovery of >90%, and an impressive cell enrichment of $>2.02 \times 10^5$ -fold. Compared with existing rare cell isolation technologies, the current microfluidic device possesses high throughput, cell recovery, and cell enrichment. In addition, the microfluidic platform was driven by purely hydrodynamic forces, which prevents the integration of complex external force fields, making the device easy to fabricate and operate. Although sample dilutions similar to existing separation technologies are required to reduce blood viscosity and avoid channel blocking, the simple channel design in the current device allows for easy multiplex cascading of separation circuits in parallel, in series, and in lamination layers, with the ability to analyze milliliters of clinical blood samples within a short period of time. Along with the trend of combining multiple rare cell separation methods on a single device, the innovative strategy of combining inertial microfluidics and steric hindrance could be used to sort a variety of rare cells with higher efficiency, indicating significant potential for numerous areas of sample preparation in fundamental studies and clinical diagnoses.

Acknowledgements

This study was supported by the National Natural Science Foundation of China (21175107 and 21375106), the Ministry of Education of the People's Republic of China (NCET-08-602 0464), the Fundamental Research Funds for the Central Universities (Z109021303), the Scientific Research Foundation for

the Returned Overseas Chinese Scholars, the State Education Ministry, and the Northwest A&F University.

Notes and references

- M. Toner and D. Irimia, *Annu. Rev. Biomed. Eng.*, 2005, **7**, 77–103.
- U. Dharmasiri, M. A. Witek, A. A. Adams and S. A. Soper, *Annu. Rev. Anal. Chem.*, 2010, **3**, 409–431.
- M. Cristofanilli, G. T. Budd, M. J. Ellis, A. Stopeck, J. Matera, M. C. Miller, J. M. Reuben, G. V. Doyle, W. J. Allard, L. M. Terstappen and D. F. Hayes, *N. Engl. J. Med.*, 2004, **351**, 781–791.
- C. Wittekind and M. Neid, *Oncology*, 2005, **69**, 14–16.
- W. J. Allard, J. Matera, M. C. Miller, M. Repollet, M. C. Connelly, C. Rao, A. G. J. Tibbe, J. W. Uhr and L. W. M. Terstappen, *Clin. Cancer Res.*, 2004, **10**, 6897–6904.
- H. W. Hou, M. E. Warkiani, B. L. Khoo, Z. R. Li, R. A. Soo, D. S.-W. Tan, W.-T. Lim, J. Han, A. A. S. Bhagat and C. T. Lim, *Sci. Rep.*, 2013, **3**, 1259.
- A. A. S. Bhagat, H. Bow, H. W. Hou, S. J. Tan, J. Han and C. T. Lim, *Med. Biol. Eng. Comput.*, 2010, **48**, 999–1014.
- R. Kalluri and R. A. Weinberg, *J. Clin. Invest.*, 2009, **119**, 1420–1428.
- C. V. Pecot, F. Z. Bischoff, J. A. Mayer, K. L. Wong, T. Pham, J. Bottsford-Miller, R. L. Stone, Y. G. Lin, P. Jaladurgam, J. W. Roh, B. W. Goodman, W. M. Merritt, T. J. Pircher, S. D. Mikolajczyk, A. M. Nick, J. Celestino, C. Eng, L. M. Ellis,

- M. T. Deavers and A. K. Sood, *Cancer Discovery*, 2011, **1**, 580–586.
- 10 L. Zhang, L. D. Ridgway, M. D. Wetzel, J. Ngo, W. Yin, D. Kumar, J. C. Goodman, M. D. Groves and D. Marchetti, *Sci. Transl. Med.*, 2013, **5**, 180ra48.
- 11 X. Mu, W. Zheng, J. Sun, W. Zhang and X. Jiang, *Small*, 2013, **9**, 9–21.
- 12 A. A. S. Bhagat, H. W. Hou, L. D. Li, C. T. Lim and J. Han, *Lab Chip*, 2011, **11**, 1870–1878.
- 13 W. Chen, S. Weng, F. Zhang, S. Allen, X. Li, L. Bao, R. H. W. Lam, J. A. Macoska, S. D. Merajver and J. Fu, *ACS Nano*, 2012, **7**, 566–575.
- 14 M. S. Kim, T. S. Sim, Y. J. Kim, S. S. Kim, H. Jeong, J.-M. Park, H.-S. Moon, S. I. Kim, O. Gurel, S. S. Lee, J.-G. Lee and J. C. Park, *Lab Chip*, 2012, **12**, 2874–2880.
- 15 H. Mohamed, M. Murray, J. N. Turner and M. Caggana, *J. Chromatogr. A*, 2009, **1216**, 8289–8295.
- 16 A. E. Saliba, L. Saias, E. Psychari, N. Minc, D. Simon, F. C. Bidard, C. Mathiot, J.-Y. Pierga, V. Fraisier, J. Salamero, V. Saada, F. Farace, P. Vielh, L. Malaquin and J.-L. Viovy, *Proc. Natl. Acad. Sci. U. S. A.*, 2010, **107**, 14524–14529.
- 17 S. K. Arya, B. Lim and A. R. A. Rahman, *Lab Chip*, 2013, **13**, 1995–2027.
- 18 D. R. Gossett, H. T. K. Tse, J. S. Dudani, K. Goda, T. A. Woods, S. W. Graves and D. Di Carlo, *Small*, 2012, **8**, 2757–2764.
- 19 G. Guan, L. Wu, A. A. S. Bhagat, Z. Li, P. C. Chen, S. Chao, C. J. Ong and J. Han, *Sci. Rep.*, 2013, **3**, 1475.
- 20 M. E. Warkiani, G. Guan, B. L. Khoo, W. C. Lee, A. A. S. Bhagat, P. K. Chaudhuri, D. S.-W. Tan, W.-T. Lim, S. C. Lee, P. C. Y. Chen, C. T. Lim and J. Han, *Lab Chip*, 2014, **14**, 128–137.
- 21 C. W. Schaeffer, A. W. Partin, W. B. Isaacs, D. S. Coffey and J. T. Isaacs, *Prostate*, 1994, **25**, 249–265.
- 22 D. Marrinucci, K. Bethel, R. H. Bruce, D. N. Curry, B. Hsieh, M. Humphrey, R. T. Krivacic, J. Kroener, L. Kroener, A. Ladanyi, N. H. Lazarus, J. Nieva and P. Kuhn, *Hum. Pathol.*, 2007, **38**, 514–519.
- 23 X. Chen, D. F. Cui, C. C. Liu and H. Li, *Sens. Actuators, B*, 2008, **130**, 216–221.
- 24 J. Sun, M. Li, C. Liu, Y. Zhang, D. Liu, W. Liu, G. Hu and X. Jiang, *Lab Chip*, 2012, **12**, 3952–3960.
- 25 H. Wei, B. Chueh, H. Wu, E. W. Hall, C. Li, R. Schirhagl, J.-M. Lin and R. N. Zare, *Lab Chip*, 2011, **11**, 238–245.
- 26 T. Gerhardt, S. Woo and H. Ma, *Lab Chip*, 2011, **11**, 2731–2737.
- 27 S. M. McFaul, B. K. Lin and H. Ma, *Lab Chip*, 2012, **12**, 2369–2376.
- 28 H.-S. Moon, K. Kwon, S.-I. Kim, H. Han, J. Sohn, S. Lee and H.-I. Jung, *Lab Chip*, 2011, **11**, 1118–1125.
- 29 A. J. Mach and D. Di Carlo, *Biotechnol. Bioeng.*, 2010, **107**, 302–311.
- 30 W. Liu, L. Li, J. C. Wang, Q. Tu, L. Ren, Y. Wang and J. Wang, *Lab Chip*, 2012, **12**, 1702–1709.
- 31 J.-S. Park and H.-I. Jung, *Anal. Chem.*, 2009, **81**, 8280–8288.
- 32 P. G. Saffman, *J. Fluid Mech.*, 1965, **22**, 385–400.
- 33 J. Zhou and I. Papautsky, *Lab Chip*, 2013, **13**, 1121–1132.
- 34 J.-S. Park, S.-H. Song and H.-I. Jung, *Lab Chip*, 2009, **9**, 939–948.
- 35 S. C. Hur, N. K. Henderson-MacLennan, E. R.B. McCabe and D. Di Carlo, *Lab Chip*, 2011, **11**, 912–920.
- 36 D. Jiang, D. Sun, N. Xiang, K. Chen, H. Yi and Z. Ni, *Biomicrofluidics*, 2013, **7**, 034113.
- 37 J. Zhang, M. Li, W. H. Li and G. Alici, *J. Micromech. Microeng.*, 2013, **23**, 085023.
- 38 L. Zeng, F. Najjar, S. Balachandar and P. Fischer, *Phys. Fluids*, 2009, **21**, 033302.
- 39 D. Di Carlo, D. Irimia, R. G. Tompkins and M. Toner, *Proc. Natl. Acad. Sci. U. S. A.*, 2007, **104**, 18892–18897.
- 40 S. L. Stott, C.-H. Hsu, D. I. Tsukrov, M. Yu, D. T. Miyamoto, B. A. Waltman, S. M. Rothenberg, A. M. Shah, M. E. Smas, G. K. Korir, F. P. Floyd, A. J. Gilman, J. B. Lord, D. Winokur, S. Springer, D. Irimia, S. Nagrath, L. V. Sequist, R. J. Lee, K. J. Isselbacher, S. Maheswaran, D. A. Haber and M. Toner, *Proc. Natl. Acad. Sci. U. S. A.*, 2010, **107**, 18392–18397.
- 41 A. J. Mach, J. H. Kim, A. Arshi, S. C. Hur and D. Di Carlo, *Lab Chip*, 2011, **11**, 2827–2834.
- 42 A. A. S. Bhagat, S. S. Kuntaegowdanahalli and I. Papautsky, *Microfluid. Nanofluid.*, 2009, **7**, 217–226.
- 43 B. Chun and A. J. C. Ladd, *Phys. Fluids*, 2006, **18**, 031704.
- 44 J. Zhou, P. V. Giridhar, S. Kasper and I. Papautsky, *Lab Chip*, 2013, **13**, 1919–1929.
- 45 T. Tanaka, T. Ishikawa, K. Numayama-Tsuruta, Y. Imai, H. Ueno, N. Matsuki and T. Yamaguchi, *Lab Chip*, 2012, **12**, 4336–4343.
- 46 K. Gotoh, *Nature*, 1970, **225**, 848–850.
- 47 R. D. Sochol, S. Li, L. P. Lee and L. Lin, *Lab Chip*, 2012, **12**, 4168–4177.
- 48 L. Wang, W. Liu, Y. Wang, J. C. Wang, Q. Tu, R. Liu and J. Wang, *Lab Chip*, 2013, **13**, 695–705.